Computer Modeling in
Engineering & Sciences

Tech Science Press

https://doi.org/10.32604/cmes.2026.083699

ARTICLE

Saturation and Hysteresis Nonlinearity Modeling of Piezoelectric Actuators Based on Hybrid-PINN Model

Chenghao Kou[1], **Zunyi Duan**[2,*], **Shengjie Wang**[1], **Jun Ma**[1], **Zhongwei Yang**[1], **Xudong Tang**[1] and **Rongchun Hu**[2]

[1]Beijing Machine and Equipment Institute, Beijing, China
[2]School of Mechanics and Transportation Engineering, Northwestern Polytechnical University, Xi'an, China

*Corresponding Author: Zunyi Duan. Email: duanzy@nwpu.edu.cn

Received: 08 April 2026; Accepted: 27 May 2026; Published: 30 June 2026

ABSTRACT: Piezoelectric actuators are widely used in precision positioning systems. However, their inherent nonlinear behaviors, particularly hysteresis and output saturation, degrade modeling accuracy and limit control performance. Existing studies have generally used either black-box models or traditional physical models. The former typically lack physical interpretability, while the latter can exhibit limited accuracy when the actuator response includes coupled nonlinear effects. To address this issue, this paper proposes a hybrid physics-informed neural network (Hybrid-PINN) framework. An equivalent attenuation model, with a calibrated attenuation coefficient, is first established to describe output saturation and provide a nominal physical reference. A parallel neural network is then introduced to compensate for higher-order residuals not accounted for by the nominal physical model. By incorporating a physically constrained loss function, the proposed framework combines information from the physical mechanism with experimental data. A series of experiments was conducted on a stacked lever-amplified piezoelectric actuator. The results show that the proposed model captures the main hysteresis and saturation tendencies of the tested actuator, and that prediction accuracy is improved by more than 20% compared with the traditional physical model. A detailed comparison with a multilayer perceptron, a standard physics-informed neural network, and LSTM models was also performed. The proposed model achieves lower prediction errors in most of the tested cases and exhibits improved convergence under current experimental conditions. Overall, this work provides a physically interpretable modeling framework at the actuator level for piezoelectric actuators within their calibrated operating range.

KEYWORDS: Piezoelectric actuators; saturation; hysteresis; Hybrid-PINN

1 Introduction

Piezoelectric actuators (PEAs) are playing an increasingly important role in modern precision engineering, primarily due to their high resolution and wide bandwidth [1]. These systems are widely used in many advanced applications requiring extreme positioning accuracy, such as semiconductor lithography, ultra-precise optical alignment [2], micro-nano-manipulation robots [3], and biomedical engineering. Compared to traditional mechanical transmission mechanisms, PEAs exploit the elastic deformation of materials to transmit motion, enabling nanometer-scale positioning accuracy [4]. However, their limitations cannot be ignored. The strong nonlinearities inherent in piezoelectric ceramic materials, such as hysteresis and creep [5,6], as well as the complex dynamic coupling and resonance of flexible mechanisms under high-frequency operating conditions [7], significantly limit the closed-loop control accuracy and the system's effective bandwidth. Therefore, establishing a high-precision, physically interpretable, and computationally efficient dynamic model is a fundamental prerequisite. Such a model provides a basis for subsequent control and error compensation.

In the field of nonlinear modeling of piezoelectric actuators, current research focuses primarily on describing and compensating for hysteresis nonlinearity. Classical phenomenological models, such as the Bouc-Wen model, the Prandtl-Ishlinskii model, and their improved versions, are widely used to describe the characteristics of the hysteresis loop. This is mainly due to their simple structure and ease of identification. Dai et al. [8] and Cai et al. [9] conducted a review of piezoelectric hysteresis modeling, highlighting the dominant role of the Bouc-Wen model due to its simplicity. To improve accuracy, some researchers, such as Liu and Zhang [10], Gu et al. [11], and Wang and Zhou [12], have introduced particle swarm or gray wolf optimization algorithms to determine the parameters of the Bouc-Wen model. To address the problem of asymmetric hysteresis characteristics, Li et al. [13] and Zhou et al. [14] proposed asymmetric Bouc-Wen models. Regarding speed-dependent characteristics, Zhu et al. [15] and Zhang et al. [16] improved the generalized PI model and the Hammerstein model, respectively. Furthermore, to describe the electromechanical coupling characteristics of piezoelectric stacks from a physical perspective, Ling et al. [17] developed an electromechanical model based on the dynamic stiffness matrix. Piezoelectric hysteresis and nonlinear response have also been studied in vibration energy harvesting. For example, frequency up-converted and magnetically plucked piezoelectric harvesters show that nonlinear deformation and magnetic interaction can affect the dynamic response even under limited electric fields [18,19]. However, most of these models focus on fitting hysteresis loops [20], while the reduction in incremental displacement gain under large-stroke operating conditions is usually treated in an empirical manner or is not explicitly represented.

Furthermore, the rapid development of artificial intelligence offers new perspectives for data-driven modeling methods to address complex nonlinear problems. Thanks to their strong nonlinear fitting capabilities, deep learning models such as recurrent neural networks (RNNs) and Long Short-Term Memory (LSTM) networks exhibit significantly higher accuracy than traditional models in modeling piezoelectric hysteresis. For example, Cheng et al. [21] and Jin et al. [22] established high-accuracy piezoelectric hysteresis models using multilayer perceptron (MLP) networks and convolutional LSTM networks, respectively. Zhu et al. [23] proposed a modeling method based on NARX neural networks to account for the influence of charge stiffness. Lu et al. [24] used a strategy combining several NARMA-L2 models to improve modeling accuracy. In addition to neural networks, Baziyad et al. [25] and Meng et al. [26] also explored certain machine learning methods, such as least-squares support vector machines and Gaussian processes. However, purely data-driven methods also have major drawbacks. Their black box nature severely limits their physical interpretability, and their generalization capacity is highly dependent on the coverage of the training data. If the system's operating conditions fall outside the training range, the model's performance drops sharply. Furthermore, it is not possible to guarantee that their outputs will always follow fundamental physical laws [27].

To effectively combine the advantages of mechanistic and data-driven models, many researchers are exploring hybrid or gray-box modeling strategies. For example, Ahmed and Yan [28] proposed a gray-box neural network method using prior physical knowledge, hoping to reduce training time and improve accuracy. Meanwhile, Chen et al. [29] developed a hybrid architecture combining a neural network with an enhanced PI model to compensate for residuals. Furthermore, Ni et al. [30] proposed a neural-enriched Duhem model, and Jin et al. [31] constructed a Hammerstein model based on optimized composite neural networks. Aggogeri and Pellegrini [32] also proposed a data-driven hybrid model using committee machines. While these methods improve system performance, most of their strategies remain simple weighted series or combinations. Recently, Physics-Informed Neural Networks (PINN) have provided an interesting perspective, allowing for the direct linking of physical laws to observed data. The standard PINN network typically incorporates physical equations into its loss function, enabling it to solve complex problems even without labeled data. However, its direct application to piezoelectric dynamics inevitably leads to serious convergence difficulties. This is primarily due to the high stiffness, rapid dynamics, complex friction, and parameter drift inherent to these systems. In this context, forcing the network to strictly satisfy these simplified physical equations only limits its accuracy and ultimately leads to undertraining.

To address the aforementioned problems, this paper proposes a hybrid physics-informed neural network (Hybrid-PINN) framework for actuator-level modeling of PEAs with a lever mechanism. The classification of mainstream modeling strategies for PEAs and the positioning of the proposed Hybrid-PINN method is shown in Fig. 1 below. First, an improved nominal model is proposed by introducing an equivalent attenuation factor to account for the reduction in actuation gain observed under large-stroke operating conditions. This factor is considered a device-level correction parameter rather than a universal material constant. Next, a parallel residual compensation architecture is used to enable a deep neural network to learn the unmodeled high-frequency dynamics that the physical model fails to capture. The experimental results show that the proposed gray-box strategy can improve the prediction accuracy in most of the tested cases, and it also helps to reduce the convergence difficulty that was observed in the standard PINN baseline.

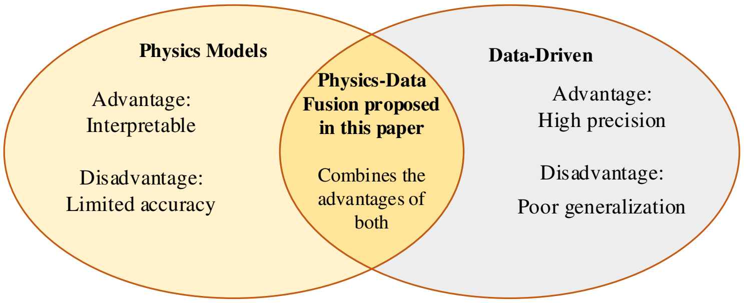

Figure 1: Classification of existing modeling approaches and the positioning of the proposed method.

For clarity, the remainder of this article is organized as follows. Section 2 presents the dynamic model of the system, taking into account the constraint coupling effect. Section 3 describes in detail the Hybrid-PINN architecture and its learning strategy. Section 4 describes the experimental platform used and validates the proposed method through the results obtained. Finally, Section 5 briefly concludes this article.

2 System Dynamic Modeling

In this section, we establish a dynamic system model for the piezoelectric actuator. Due to the complex nonlinear characteristics under conditions of long stroke and high dynamics, preliminary experiments show the presence of output saturation. Furthermore, taking into account the complex electromechanical coupling and the nonlinearity of contact friction during actual operation, we perform detailed calculations from three perspectives: mechanical dynamics, piezoelectric actuation mechanisms, and hysteresis nonlinearity. These considerations lead to a lumped dynamic equation that is used as the nominal physical model in the subsequent hybrid identification framework.

2.1 Preliminary Experimental Observation

Before proceeding with the detailed physical modeling, we performed a quasi-static open-loop test on the piezoelectric micro-positioning platform. This test aimed to clarify the nonlinear behavior of the system under long-stroke conditions. The signal used was a sinusoidal voltage with an amplitude between 0 and

40 V, at a frequency of 0.5 Hz. The experimentally obtained displacement-voltage characteristic curve is shown in Fig. 2 below.

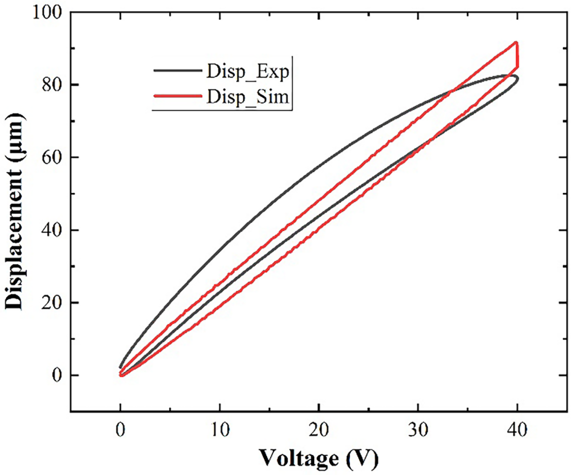

Figure 2: Comparison between linear model prediction and experimental data.

As can be seen, the solid black line represents the experimental data, while the solid red line corresponds to the prediction results based on the Bouc-Wen piezoelectric equation. Comparing these two curves highlights two important phenomena: hysteresis nonlinearity and output saturation. Hysteresis nonlinearity is characterized by the non-coincidence of the ascending and descending branches, forming a very distinct hysteresis loop, which constitutes an intrinsic memory characteristic of piezoelectric ceramics. Output saturation refers to the reduction in the incremental displacement gain of PEAs under large-voltage or large-stroke operation, characterized by a decreasing slope of the voltage–displacement curve as the input approaches the upper end of the operating range [33]. This is distinct from voltage amplifier saturation, input clipping, or stroke limitation imposed by driving electronics. In this work, output saturation is treated as a device-level electromechanical nonlinearity associated with reduced actuation gain under large-stroke operation.

The term large-stroke operation is used in a relative sense in this paper, referring to the condition in which the actuator output displacement is large enough that the linear voltage–displacement relation is no longer sufficient to describe the measured response with acceptable accuracy. It does not imply that the piezoelectric stack has reached its mechanical travel limit. The model developed in this paper is applicable to stacked piezoelectric actuators with external lever mechanisms, and its direct applicability is limited to such lumped axial actuation systems.

These phenomena indicate that traditional linear piezoelectric models lack accuracy. Furthermore, this type of nonlinearity cannot be ascribed solely to the geometric nonlinearity of the mechanical structure. Indeed, flexible hinges remain within the linear elastic range even when subjected to micron-scale deformation. These observations indicate that the linear voltage–displacement relation is not accurate enough in the large-stroke region. In this work, the reduction in displacement gain observed from the experiments is used as the motivation to introduce an equivalent attenuation term into the nominal device-level model.

2.2 Mechanical Dynamic Model

Before proceeding with the detailed dynamic analysis, it is necessary to simplify the physical system. Considering that the first resonant frequency of the actuator is significantly lower than that of higher-order modes, and that its operating bandwidth lies primarily in the low frequencies, a lumped-parameter model was adopted. This method allows us to model the complex flexible mechanism as a mass-spring-damper system with a single degree of freedom. The precise model and its structural diagram are presented in detail in Fig. 3 below.

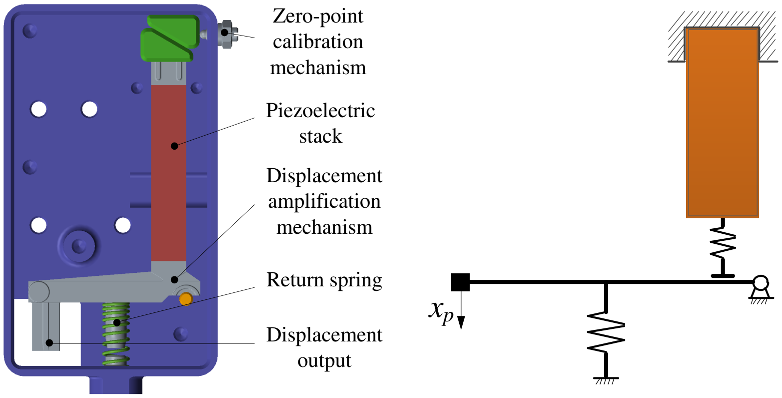

Figure 3: 3D model and working mechanism schematic of the lever-amplified piezoelectric actuator.

Let $x(t)$ be the output displacement of the actuator. According to Newton's second law, the equilibrium equation for the forces at the output is written as

$$m_{eq}\ddot{x}(t) + c_{eq}\dot{x}(t) + F_{res}(t) = F_{drive}(t), \tag{1}$$

where m_{eq} represents the equivalent mass of the system with respect to the output. It incorporates the mass of the terminal load as well as the equivalent moment of inertia of the moving components, such as the lever arm and flexible joints. The parameter c_{eq} represents the equivalent viscous damping coefficient. It characterizes the energy dissipation due primarily to the internal damping of the material and damping by air, and is assumed to be proportional to the velocity $\dot{x}(t)$. Finally, $F_{res}(t)$ represents the total resistance force encountered by the system during its motion, composed mainly of the elastic restoring force and contact friction.

$$F_{res}(t) = F_{spring}(t) + F_{friction}(t). \tag{2}$$

The friction force $F_{friction}(t)$ arises primarily from the interaction between the guiding or contact components. To avoid the problem of numerical discontinuity in the classical Coulomb friction model at zero velocity, we opted for a hyperbolic tangent function model to describe this behavior:

$$F_{friction}(t) = f_f \tanh(\sigma\dot{x}(t)), \tag{3}$$

where f_f represents the maximum amplitude of static friction. The factor σ, is a smoothing factor used to control the slope of the friction force transition at the zero crossing.

2.3 Equivalent Attenuation Model

$F_{drive}(t)$ represents the effective driving force transmitted from the piezoelectric stack to the output end via the lever mechanism. Most existing modeling methods generally assume that the piezoelectric strain constant d_{33} is constant. This assumption implies a proportional relationship between the output force and the voltage. However, experimental results exhibit an obvious discrepancy. The slope of the displacement-voltage curve decreases with increasing excitation voltage and output displacement. This indicates an output-gain attenuation trend in the large-stroke region.

From the perspective of the device, the saturation phenomenon could be understood as a decrease in the incremental actuation gain during large-stroke operations. This kind of reduction is probably related to the mechanical boundary constraints, the variation of preload, the electromechanical response that depends on stress, along with some other unmodeled coupling effects. Because it is quite difficult to separate these internal mechanisms merely based on the input-output displacement data, an equivalent displacement-dependent attenuation term is introduced here to represent all of them. This equivalent treatment is schematically illustrated in Fig. 4.

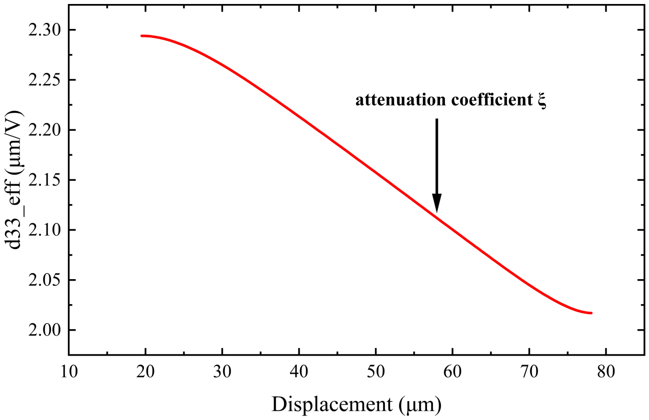

Figure 4: The attenuation curve of the effective piezoelectric coefficient d_{33}^{eff} vs. displacement.

In order to express this observed gain attenuation phenomenon in a compact way, we introduce an equivalent actuation coefficient that depends on the displacement into the nominal model. It should be noted that the main purpose of this coefficient is not trying to replace the intrinsic material constant d_{33}. On the contrary, it is used to describe the reduction of actuation gain from the device level under the operating range we tested.

$$d_{33}^{eff}(x) = d_{33} - \xi|x(t)|, \tag{4}$$

where ξ is an attenuation coefficient obtained by parameter identification. Under this mathematical formulation, d_{33}^{eff} is supposed to be understood as a kind of equivalent actuation gain, instead of the intrinsic constant of the piezoelectric material. Specifically, a larger value of $|x(t)|$ will result in a smaller equivalent gain in the nominal model. This formulation represents the measured decrease in the voltage–displacement slope in a compact form.

According to the principle of differential impedance, the internal driving force generated by the piezoelectric stack depends primarily on the difference between its theoretical no-load elongation and its actual elongation under load. Therefore, after incorporating the previously mentioned attenuation model, the theoretical no-load elongation must be corrected as

$$x_{pz}^{theory}(t) = d_{33}^{eff}(x) \cdot u(t) - h(t) = (d_{33} - \xi|x(t)|)\, u(t) - h(t), \tag{5}$$

where $u(t)$ represents the input voltage and $h(t)$ the hysteresis variable. Then, again based on the principle of differential impedance, and taking into account the finite stiffness K_p of the piezoelectric stack and the gain ratio i_{ratio}. The gain ratio is a dimensionless effective mechanical amplification factor for the lever mechanism. It considers the geometric amplification caused by the lever structure, as well as the possible compliance loss along the transmission path. In this study, i_{ratio} is used to convert the axial deformation produced by the piezoelectric stack into the measured output displacement of the actuator assembly.

The effective driving force acting on the output mass can finally be expressed as

$$F_{drive}\left(t\right) = \frac{K_p}{i_{ratio}}\left(\underbrace{d_{33}u\left(t\right)}_{Linear\ actuation} - \underbrace{\xi\left|x\left(t\right)\right|u\left(t\right)}_{Equivalent\ attenuation\ correction} - h\left(t\right) - \frac{x\left(t\right)}{i_{ratio}}\right). \tag{6}$$

As shown in Eq. (6), the specific mathematical term $-\xi\left|x\left(t\right)\right|u\left(t\right)$ will lead to the reduction of the equivalent actuation gain, along with the continuous increasing of the displacement and the voltage. Consequently, it offers a compact phenomenological method to represent the attenuation phenomenon of the slope which we have already observed from the voltage-displacement curve. The main reason why we adopt this kind of treatment is to maintain the nominal model at a relatively low-order level, making it easy to be identified merely based on the input-output data. Meanwhile, as for the remaining dynamics that are not modeled, they will be handled by the residual learning component.

In the present model, only the dominant d_{33} mode is retained because the tested device is a stacked piezoelectric actuator whose main displacement follows the direction of polarization. Under this axial configuration, the longitudinal electromechanical coupling mainly governs the nominal input-output relation. Therefore, the transverse strain related to d_{31} is not explicitly included in the dynamic equation. Instead, its possible influence, together with the lever compliance, boundary constraints, and other transverse effects, are all absorbed into the equivalent parameters. It must be pointed out that this simplification is only suitable for the stacked actuator studied here, and cannot be generalized directly to other configurations.

It is necessary to point out that the attenuation formulation we proposed is an equivalent treatment, instead of a nonlinear electro-elastic constitutive law. For those models that are based on the energy density, they usually describe the nonlinearity of the material at the constitutive level. Therefore, they are much more suitable for the distributed piezoelectric structures, or the structures dominated by bending, such as the bimorph beams and piezoelectric patches [34]. However, the attenuation coefficient is only utilized to represent the saturation trend of the stacked piezoelectric actuator that we measured, under the calibrated operating range.

2.4 Bouc-Wen Hysteresis Model

To accurately describe the inherent nonlinearity of hysteresis and the loop memory effect in the displacement-voltage curve, this article uses the classical Bouc-Wen model for the dynamic evolution of the hysteresis variable $h\left(t\right)$. This phenomenological model, widely used in the field of smart materials modeling, employs differential equations to accurately describe smooth hysteresis loops of various shapes.

The specific evolution equation for the hysteresis variable $h\left(t\right)$ is defined as

$$\dot{h}\left(t\right) = \alpha\dot{u}\left(t\right) - \beta\left|\dot{u}\left(t\right)\right|\left|h\left(t\right)\right|^{n-1}h\left(t\right) - \gamma\dot{u}\left(t\right)\left|h\left(t\right)\right|^{n}, \tag{7}$$

where α primarily controls the amplitude of the linear response to the input voltage. The parameters β and γ control the shape, width, and asymmetry of the loop. Finally, the parameter n controls the smoothness of the transition between the elastic and plastic phases. For example, the model exhibits a gradual nonlinear transition for $n = 1$. Conversely, a very high value of n results in an abrupt transition, characteristic of elastoplastic materials.

Furthermore, the Bouc-Wen model incorporates the input voltage history to effectively reflect the delay effect of the internal domain bias. Under the framework mentioned above, the Bouc-Wen model is utilized to describe the width of the loop and the phenomenon of memory effect. At the same time, the equivalent attenuation term, which we have introduced in the previous section, is applied to represent the saturation tendency of the skeleton curve.

2.5 Overall System Dynamic Equation

By combining the previously mentioned mechanical dynamic equation, the piezoelectric drive equation coupled to the constraints, and the nonlinear hysteresis equation, we obtain the complete dynamic description of the system.

$$\begin{cases} m_{eq}\ddot{x} + c_{eq}\dot{x} + F_{res\_total}\left(x, \dot{x}\right) = \frac{K_p}{i_{ratio}}\left(\left(d_{33} - \xi|x|\right)u - h\right). \\ \dot{h} = \alpha\dot{u} - \beta|\dot{u}||h|^{n-1}h - \gamma\dot{u}|h|^{n} \end{cases} \tag{8}$$

To simplify the expression, we use the term total impedance force F_{res_total} to encompass the mechanical stiffness, the internal piezoelectric stiffness related to the lever, and the friction force:

$$F_{res\_total} = \left(\frac{1}{2}K_{spr} + \frac{K_p}{i_{ratio}^2}\right)x + f_f \tanh\left(\sigma\dot{x}\right). \tag{9}$$

The resulting nominal model includes inertia, viscous damping, friction regularization, equivalent actuation attenuation, and hysteresis memory. It is used as the physical reference in the subsequent hybrid identification framework. However, it must be acknowledged that real piezoelectric systems generally contain high-order nonlinear factors that are extremely difficult to model analytically. These factors include, in particular, frequency-dependent hysteresis, complex friction, and measurement noise. Under certain specific operating conditions, these unmodeled dynamics will inevitably lead to small residuals in the physical model.

3 Hybrid Physics-Informed Neural Network Identification Method

3.1 Hybrid Modeling Architecture

In this chapter, to improve accuracy and generalization, we propose a physics-informed hybrid neural network identification method. This method relies primarily on a parallel compensation strategy. More specifically, the physical model constitutes the main component, while the neural network plays an important role as an auxiliary component. The following section describes in detail the overall architecture, data preprocessing, network structure, and the physics-constrained loss function.

Unlike black box models that completely ignore physics, or standard PINNs that use physics only for regularization, Hybrid-PINN adopts a parallel residual compensation architecture of the gray box type, as illustrated in Fig. 5.

The predicted total displacement $\hat{x}\left(t\right)$ is decomposed into two parts: a nominal physical component and a residual compensation component.

$$\hat{x}\left(t\right) = x_{nom}\left(t\right) + x_{res}\left(t\right). \tag{10}$$

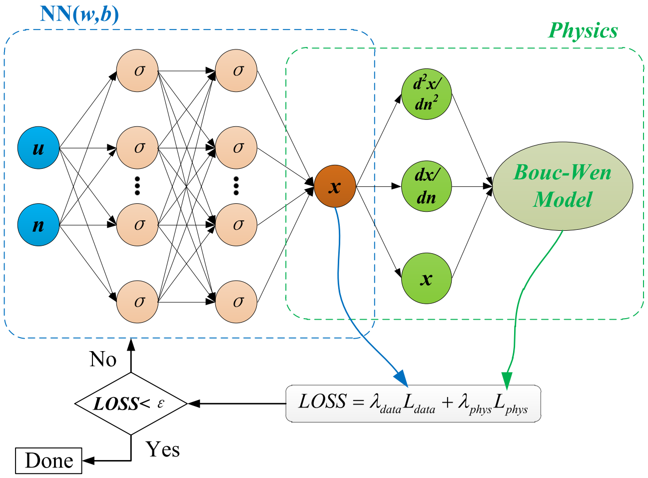

Figure 5: Overall architecture of the proposed Hybrid-PINN.

Initially, the nominal physical component $x_{nom}(t)$ is derived from the equivalent attenuation model presented in Section 2. By doing this, the proposed model has the capability to describe the dominant changing trend of the hysteresis loop, as well as the saturation phenomenon of the output. Therefore, it can be regarded as a nominal physical reference aiming at the compensation of the residuals. The $x_{res}(t)$ residual compensation component, on the other hand, comes from the neural network. It allows us to capture small, high-order errors that are unfortunately undetected by the pure physical model.

This architecture allows the network to focus on fitting small residuals, rather than learning fundamental physical laws. Consequently, this method reduces the learning difficulty and accelerates convergence. This architecture is expected to improve physical consistency compared with a purely data-driven model.

3.2 Data Preprocessing and Normalization

During hybrid modeling, we observe that the input variables (such as time t and voltage u) and the output variables (displacement x) have very different physical orders of magnitude. This difference is likely to cause numerical instability during backpropagation, often leading to the disappearance or explosion of the gradient, which seriously compromises the model's convergence. Therefore, all input and output variables were normalized. The normalization and denormalization procedure is illustrated in Fig. 6.

First, the input variable vector $\mathbf{X} = [t, u, \dot{u}]^T$ is transformed in the interval [−1, 1] using the Max-Min normalization method as

$$\hat{u} = \frac{u - u_{min}}{u_{max} - u_{min}}, \quad \widehat{\dot{u}} = \frac{\dot{u} - \dot{u}_{min}}{\dot{u}_{max} - \dot{u}_{min}}. \tag{11}$$

Second, the output displacement x is multiplied by a factor λ_{scale}. We proceed in this way to keep the network output within the sensitive range of the Tanh activation function:

$$\hat{x}_{res} = \frac{x_{res}}{\lambda_{scale}}. \tag{12}$$

Finally, the actual physical prediction is obtained by an inverse output transformation as

$$x_{res}^{pred} = \mathcal{N}\left(\hat{t}, \hat{u}, \widehat{\dot{u}}; \theta\right) \cdot \lambda_{scale}, \tag{13}$$

where $\mathcal{N}(\cdot)$ represents the network mapping function and θ represents the network weights.

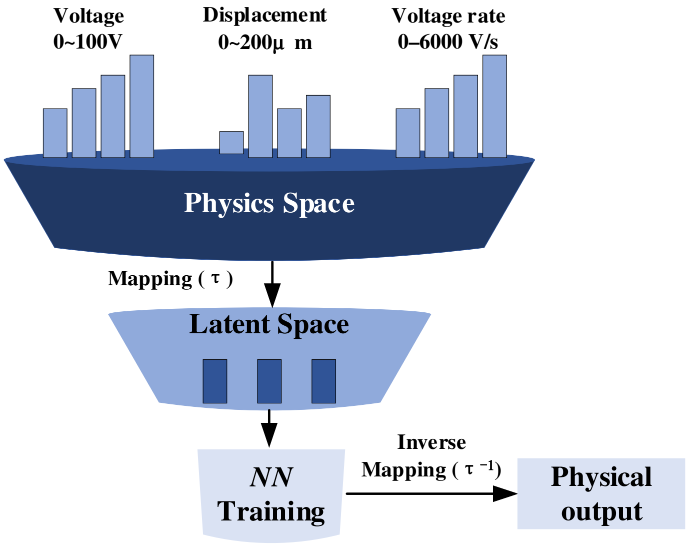

Figure 6: Data flow of the normalization and denormalization process.

The normalization is just used as a numerical scaling procedure for the training of neural network and the evaluation of loss function. It will not make any change to the physical stiffness, mass, damping, or rigid dynamic properties of PEAs. The normalization constants are calculated from the training data, and then kept fixed during the whole validation and testing stage, which means no information from the test data is used to update the scaling range. However, we should also be aware that if the load condition changes and this causes the effective mass, stiffness, or displacement range to shift, then these same normalization constants may no longer be able to cover the new dynamic range properly. In this situation, normalization itself is not enough to fix the mismatch problem. If such load variation happens, the nominal physical parameters need to be re-identified, or alternatively, the load-related variable should be added as an extra input to the model.

3.3 Residual Neural Network Design

A fully connected, feedforward deep neural network is constructed to adjust residuals. The input layer receives the normalized time t, voltage u, and its rate $\dot{u}$ to capture dynamic memory. The output layer provides a single scalar value, directly representing the predicted residual displacement $\hat{x}_{res}$. Fig. 7 clearly illustrates the structure of this network.

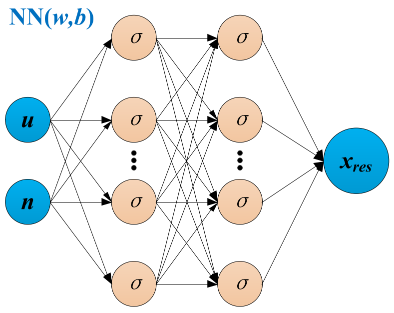

Figure 7: Structure of the feedforward deep neural network used for residual compensation.

The specific design of hidden layers is described below:

- Layers and Nodes: The residual network in the final Hybrid-PINN model contains 4 hidden layers, with 128 neurons in each hidden layer. The adopted network architecture is justified via the ablation analysis of network configurations presented in subsequent sections.
- Activation Function: The hyperbolic tangent function (Tanh) is used primarily due to the regular nature of the piezoelectric hysteresis. Unlike the ReLU, the Tanh is infinitely differentiable and is well-suited to physical problems with high-order derivatives.
- Initialization strategy: All weights and biases in the last layer are initialized to zero. In this case, the network output is initially zero, making the total prediction exactly equal to the nominal physical model. The network will then gradually learn to correct the errors in this physical model.

3.4 Physics-Constrained Loss Function

In the proposed framework, the most important element of the Hybrid-PINN network lies in the design of its loss function. Unlike standard networks that rely solely on data error, the method integrates the dynamic residuals from Section 2 into the loss function. This provides dual supervision, based on both data and physics.

More precisely, the total loss function is calculated as the weighted sum of the data and physics losses:

$$\mathcal{L}_{total} = w_{data}\mathcal{L}_{data} + w_{phys}\mathcal{L}_{physics}. \tag{14}$$

3.4.1 Data-Based Loss

Initially, the data-based loss $\mathcal{L}_{data}$ measures the difference between the total predicted output $\hat{x} = x_{nom} + \hat{x}_{res}$ and actual experimental value x_{exp}:

$$\mathcal{L}_{data} = \frac{1}{N_d}\sum_{i=1}^{N_d}\left\|\left(x_{nom}^{(i)} + \hat{x}_{res}^{(i)}\right) - x_{exp}^{(i)}\right\|^2, \tag{15}$$

where N_d represents the total number of training samples. The addition of this specific term constrains the neural network to compensate for errors in the physical model.

3.4.2 Loss of Physical Consistency

To penalize deviations from the nominal dynamic equation, the predicted displacement is substituted into the governing equation. Automatic differentiation is used to compute the velocity and acceleration terms.

The specific physical residual is thus defined as

$$f_{dyn} = F_{drive}\left(\hat{x}, u\right) - \left(m_{eq}\hat{a} + c_{eq}\hat{v} + F_{res}\left(\hat{x}, \hat{v}\right)\right). \tag{16}$$

The final physical loss function is therefore given by

$$\mathcal{L}_{physics} = \frac{1}{N_p}\sum_{j=1}^{N_p}\left\|f_{dyn}\left(t_j, \hat{x}_j, \hat{v}_j, \hat{a}_j\right)\right\|^2, \tag{17}$$

where N_p represents the total number of physical collocation points.

3.4.3 Weight Adjustment Strategy

In the hybrid architecture, since the physical model x_{nom} already provides a relatively accurate solution, the physical loss $\mathcal{L}_{physics}$ can be extremely low during the initial training phase. To encourage the neural network to better reproduce the details of the experimental data, we opted for a data weighting strategy. This strategy treats the physical equations as a soft constraint or regularization term. Furthermore, it effectively prevents overfitting in data-sparse regions and allows the model to compensate, to some extent, for uncertainties in the physical parameters. In the implementation, the data-loss weight was fixed as $w_{data} = 1$, and the relative physical-loss weight was defined as $\lambda_{phys} = w_{phys}/w_{data}$.

3.5 Optimization and Training

The model training process mainly uses a gradient-based optimization algorithm. To achieve rapid descent during the initial training phase and optimal convergence thereafter, we opted for the Adam optimizer. The entire training process is performed within the PyTorch deep learning framework. The total loss function $\mathcal{L}_{total}$ is minimized using the backpropagation algorithm and then used to iteratively update the weight parameters θ of the neural network.

In summary, this section describes the construction of the Hybrid-PINN framework. The use of a normalization method allows us to resolve the numerical difficulties associated with coupling multiple physical quantities. Furthermore, the parallel residual architecture ensures efficient merging of physical mechanisms and data characteristics. This framework thus provides the methodological basis for the subsequent experimental validation.

4 Experimental Verification and Analysis of Results

To comprehensively evaluate the effectiveness of the Hybrid-PINN identification framework proposed in this article, we constructed an experimental platform for a piezoelectric actuator and carefully designed the system model identification and validation experiments. In the following sections, we will first present the hardware configuration and data acquisition scheme of the experimental system. Next, we will present in detail the results of the identification of the nominal physical model parameters. Finally, we will evaluate the performance of the proposed Hybrid-PINN model through several series of comparative experiments, primarily from the perspective of time tracking accuracy, error distribution characteristics, and data efficiency.

4.1 Experimental Platform Configuration

The specific experimental configuration is clearly illustrated in Fig. 8. The system under test is an integrated piezoelectric actuator. Its driving element is a stacked ceramic piezoelectric actuator (Model: NAC2015-H50, CoreMorrow), with a nominal stroke of 79.2 μm. Furthermore, a lever mechanism is used to linearly amplify the output displacement, with a designed amplification ratio of exactly 8. As a result, the amplified nominal stroke of the piezoelectric actuator is 633.6 μm.

In the experiment, the system primarily consists of three modules: signal excitation, power control, and data acquisition. The excitation signals are generated by a function generator that directly produces the control voltage waveforms with predefined frequencies and amplitudes. This low-voltage control signal is then applied to the drive controller. Powered by a high-voltage source, the controller amplifies the signal and applies it to the piezoelectric actuator, thus inducing displacement.

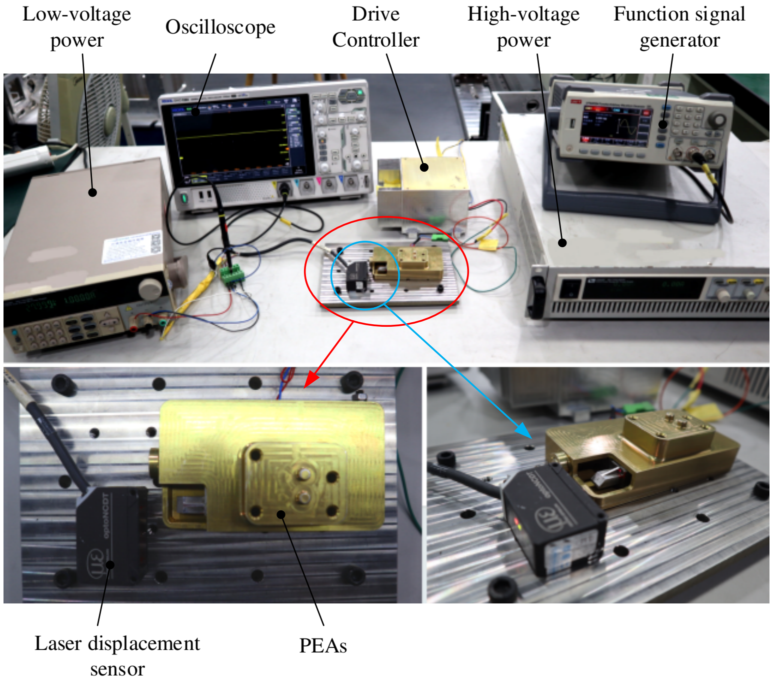

Figure 8: Photograph of the experimental setup for the PEAs.

For measurement, we use a high-precision laser displacement sensor (Model: ILD1320 10, Micro Epsilon) to monitor the actuator's output in real time and without contact. Thanks to its high repeatability of 1 μm, this sensor accurately captures the details of the micro-actuator's dynamic response. Furthermore, the sensor is powered by a low-voltage source. The analog signal from the sensor is directly connected to an oscilloscope, which is used for data acquisition and recording. To ensure that the identification data captures sufficient high-frequency dynamic information, the sampling frequency is set at 10 kHz. The operating diagram of the experimental setup is shown in Fig. 9.

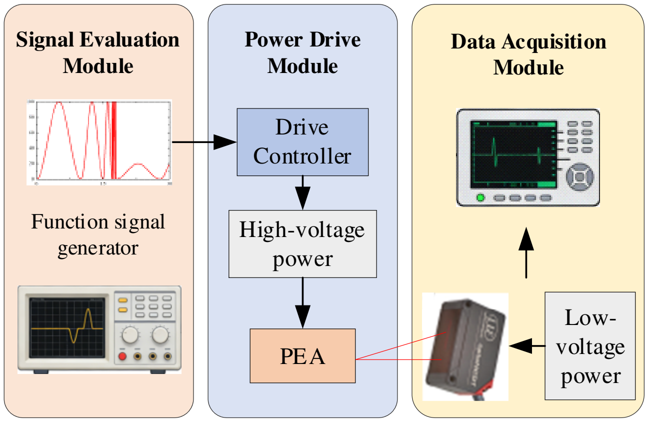

Figure 9: Operating diagram of the experimental setup.

4.2 Dataset Construction and Preprocessing

As is well known, a high-quality dataset is essential for successful data-driven modeling. To highlight the memory characteristics of the hysteresis loop and the output saturation phenomenon, we carefully designed a composite excitation signal rich in frequency and amplitude components for the drive system.

Specifically, we opted for a variable-frequency sinusoidal sweep signal. Its voltage amplitude ranges from 0 to 100 V and its frequency from 0.1 to 50 Hz. These parameters cover the main operating bandwidth of the piezoelectric actuator. The waveform of this signal is clearly visible in Fig. 10. The detailed dataset partition, including the training conditions, validation conditions, and hold-out test cases, is provided in the Supplementary Materials.

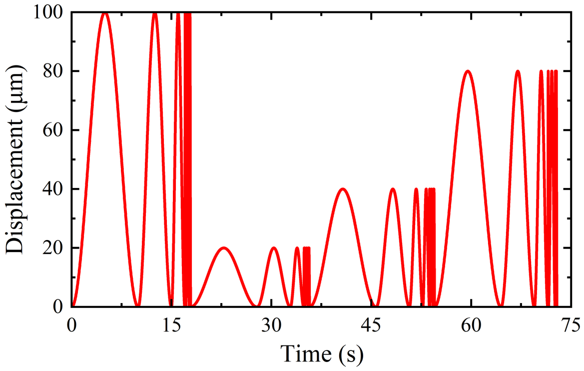

Figure 10: Specific time-domain waveforms of the excitation voltage signals used to train proposed model.

In this work, the dataset is partitioned in terms of operating conditions. Several typical voltage–frequency cases are selected as hold-out test conditions and are excluded from the training of the residual network.

To eliminate amplitude discrepancies between the voltage, displacement, and mechanical parameters, all input and output data were normalized using the Min-Max method, reducing them to the interval $[-1, 1]$. This step ensures the numerical stability of the gradient descent algorithm during training.

4.3 Identified Equivalent Parameters of the Nominal Physical Model

Before beginning the training of the hybrid network, it is essential to accurately determine the physical parameters of the previously established equivalent attenuation model. To establish the nominal model of the system, we chose the differential evolution algorithm as the global optimizer. Its objective function is defined to minimize the root mean square error (RMSE) between the simulation results of the physical model and experimental training data.

After the calculation, all the identified key physical parameters are listed in Table 1. Through the parameter identification process, the specific value of the attenuation coefficient ξ is calculated as 3.41×10^{-4}. The positive value of ξ indicates that introducing a displacement-dependent equivalent gain attenuation improves the representation of the measured large-stroke response. Additional parameter-identification results and sensitivity checks are provided in the Supplementary Materials.

Table 1: Values of all physical parameters identified in study.

Parameter Symbol	Parameter Name	Identified Value
K_{spr}	Equivalent stiffness	1.11e4 N/m
K_p	Piezoelectric stack stiffness	4.113e7 N/m
d_{33}	Nominal piezoelectric strain constant	0.308 μm/V
c_{eq}	Equivalent viscous damping coefficient	1.148e2 Ns/m
f_f	Maximum static friction force	9.544e−1 N
i_{ratio}	Lever amplification ratio	8.466
α	Linear stiffness coefficient	3.216 μm/V
β	Hysteresis hardening coefficient	1.279e2
γ	Hysteresis softening coefficient	−1.022e2
n	Hysteresis shape exponent	1.902
ξ	Equivalent attenuation coefficient	3.41e−4

As can be seen, Figs. 11 and 12 primarily illustrate the comparison of hysteresis loops and error distributions between the nominal physical model and the traditional linear model under large-stroke operating conditions (0.5 Hz). These results clearly indicate that the linear model deviates significantly from the actual experimental curve in the high-voltage region and exhibits a simple parasitic linear increase. In contrast, the nominal model, which incorporates the equivalent attenuation correction, better represents the saturation tendency near the high-voltage region. Therefore, these results demonstrate that the proposed physical model represents the dominant nonlinear dynamics of the system, thus providing a calibrated physical reference for the subsequent hybrid modeling work.

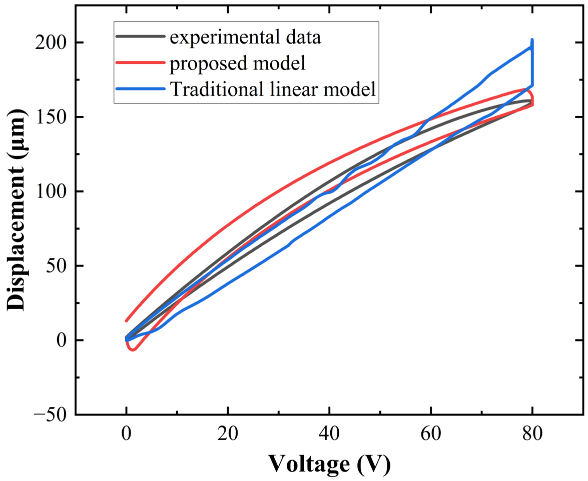

Figure 11: Comparison of hysteresis loops between experimental data and proposed model predictions at 0.5 Hz, 80 V.

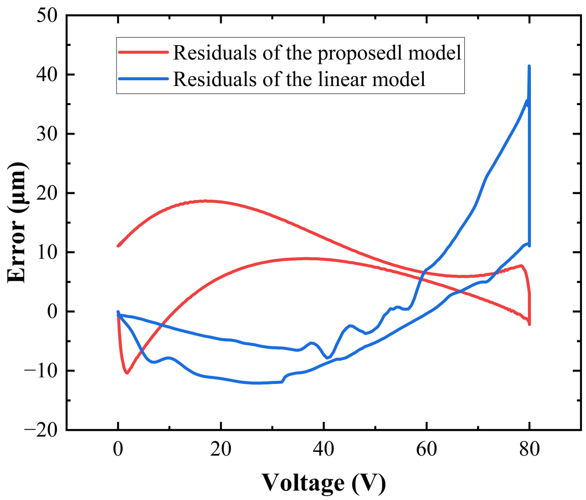

Figure 12: Detailed distribution of modeling errors for the traditional linear model and proposed model.

In order to make a further clarification for the role of these equivalent parameters, we conducted three limited checks after the process of parameter identification. Firstly, the attenuation coefficient ξ was examined under four different frequency bands, namely 0.1–1, 1–5, 5–20, and 20–50 Hz. It can be found that the maximum relative deviation among those identified band-wise values reached 193.33%. This result indicates that ξ is not supposed to be regarded as a material parameter which is invariant with the frequency. On the contrary, it is used here as an averaged equivalent attenuation coefficient under the range of voltage and frequency that we tested. Therefore, an attenuation term which is dependent on the frequency may be required, when the actuator is modeled over a wider bandwidth or under some different conditions of preload.

We also conducted an investigation where the friction smoothing factor σ in the term of $\tanh(\sigma\dot{x})$ was varied around its nominal value. It can be obviously found that when the value of σ was changed from 0.05 to 0.2, the validation RMSE of the nominal model basically remained unchanged, which only ranged from 48.447 to 48.448 μm. This experimental result suggests that the overall prediction for displacement is not dominated by this kind of smoothing treatment. Therefore, σ is used as a numerical regularization parameter to avoid the discontinuity phenomenon of the ideal Coulomb friction when it is near the zero velocity, instead of being treated as a physical friction parameter that is precisely identified.

The parameters of the Bouc-Wen model were perturbed both individually and jointly within the range of ±5% and ±10%. According to the results, it can be seen that the relative change of the RMSE basically remained within a very small range from −0.07% to 0.21%. This kind of small variation indicates that the nominal prediction is not highly dependent on a single set of fitted Bouc-Wen parameters. Therefore, these Bouc-Wen parameters are mainly utilized to describe the equivalent shape of the hysteresis loop and the phenomenon of memory effect, instead of being treated as the unique properties of the material.

4.4 Hybrid-PINN Model Performance Evaluation

To examine whether the originally used deep residual network was necessary, six network architectures were compared under the same training protocol, physical-loss weight, optimizer, and validation dataset. The tested architectures were 2 × 32, 3 × 64, 4 × 64, 4 × 128, 6 × 128, and 8 × 128, where the first number denotes the number of hidden layers and the second number denotes the number of neurons in each hidden layer. The comparison metrics include the RMSE, Mean absolute error (MAE), trainable parameter number, training time, and single-sample inference time. The complete numerical results for different network architectures and physical-loss weights are listed in the Supplementary Materials.

As is shown in Table 2, the continuous increasing of the depth of the residual network does not improve the accuracy of prediction monotonically. Among all the candidates we tested, the architecture of 4 × 128 provides the lowest mean RMSE which is 9.906 µm, as well as the lowest mean MAE of 8.259 µm. On the contrary, although the architecture of 8 × 128 contains 116,225 parameters that can be trained, and its inference time for a single sample is 0.740 ms, its mean RMSE increases to 10.405 µm. By comparing with the 8 × 128 network, the 4 × 128 network reduces the number of trainable parameters by approximately 56.8%, and the time of inference by about 29.9%. At the same time, it also produces a lower error of validation. Therefore, we finally adopt the 4 × 128 configuration for the residual network.

Table 2: Ablation study of the residual network architecture.

Architecture	Parameters	RMSE (µm)	MAE (µm)	Training Time (s)	Inference Time (ms)
2 × 32	1217	10.229	8.494	700.28	0.403
3 × 64	8641	9.954	8.352	803.77	0.465
4 × 64	12,801	10.253	8.778	921.93	0.498
4 × 128	50,177	9.906	8.259	929.44	0.519
6 × 128	83,201	10.324	8.425	1170.18	0.630
8 × 128	116,225	10.405	8.474	1421.38	0.740

The inference time we reported here merely refers to the forward computation of a single sample for the residual-network component. Therefore, it is not supposed to be interpreted as the end-to-end latency of a complete closed-loop controller at the kHz-level. A real closed-loop system would also involve the process of sensing, the preprocessing, the updating of the controller, the communication, and the dynamics of the actuator-drive. Since the present work mainly focuses on the modeling and the prediction for the nonlinear actuator, the end-to-end latency of a complete closed-loop implementation in real-time has not been evaluated yet in this paper.

In order to determine the specific weight of the physical residual term, the ratio $\lambda_{phys} = w_{phys}/w_{data}$ was varied continuously, under the condition that the architecture of the residual network was kept fixed as 4 × 128. The specific values we tested in the experiment include 0, 10^{-4}, 10^{-3}, 10^{-2}, 10^{-1}, and 1. For every single case, three different random seeds were utilized to make an evaluation for the repeatability of final result. It should be noted that, the special case where $\lambda_{phys} = 0$ represents the process of residual learning without any physical regularization.

As is shown in Table 3, along with the continuous increasing of λ_{phys}, the error of prediction does not decrease monotonically. It can be found that the lowest mean RMSE is obtained when the value of λ_{phys} is set to 10^{-2}. However, the improvement compared with the condition where $\lambda_{phys} = 0$ is quite limited, which only shows a reduction of 0.45% for the RMSE. On the contrary, larger weights of the physical loss can obviously result in the degradation of the prediction accuracy. The RMSE increases by 14.60% at $\lambda_{phys} = 10^{-1}$, and it even increases by 24.72% at $\lambda_{phys} = 1$. Consequently, the specific value of $\lambda_{phys} = 10^{-2}$ is finally adopted in proposed Hybrid-PINN model.

After setting the parameters of the nominal model, we trained the residual compensation network using the PyTorch deep learning framework. We carefully selected the Tanh activation function. To optimize the training, we used the Adam optimizer, with an initial learning rate set to 1×10^{-6} and a total of 100,000 epochs.

Table 3: Sensitivity analysis of the loss-weight ratio.

$\lambda_{phys} = w_{phys}/w_{data}$	RMSE/μm	MAE/μm	Physics Loss	Time/ms
0	10.0502 ± 0.1513	8.4566 ± 0.1620	2.9745 ± 4.1045	0.5223 ± 0.0310
10^{-4}	10.0510 ± 0.1512	8.4583 ± 0.1649	2.9645 ± 4.0898	0.5155 ± 0.0212
10^{-3}	10.0415 ± 0.1827	8.5164 ± 0.3668	0.7777 ± 0.4145	0.5126 ± 0.0161
10^{-2}	10.0050 ± 0.1047	8.4369 ± 0.1583	0.8926 ± 0.0650	0.5097 ± 0.0168
10^{-1}	11.5178 ± 0.1101	9.4522 ± 0.1327	0.0647 ± 0.0212	0.5733 ± 0.0113
1	12.5342 ± 0.0238	10.5423 ± 0.0244	0.0182 ± 0.0213	0.6210 ± 0.0271

The trained Hybrid-PINN model was then applied to the test set. The results of the time tracking are shown in Fig. 13 below.

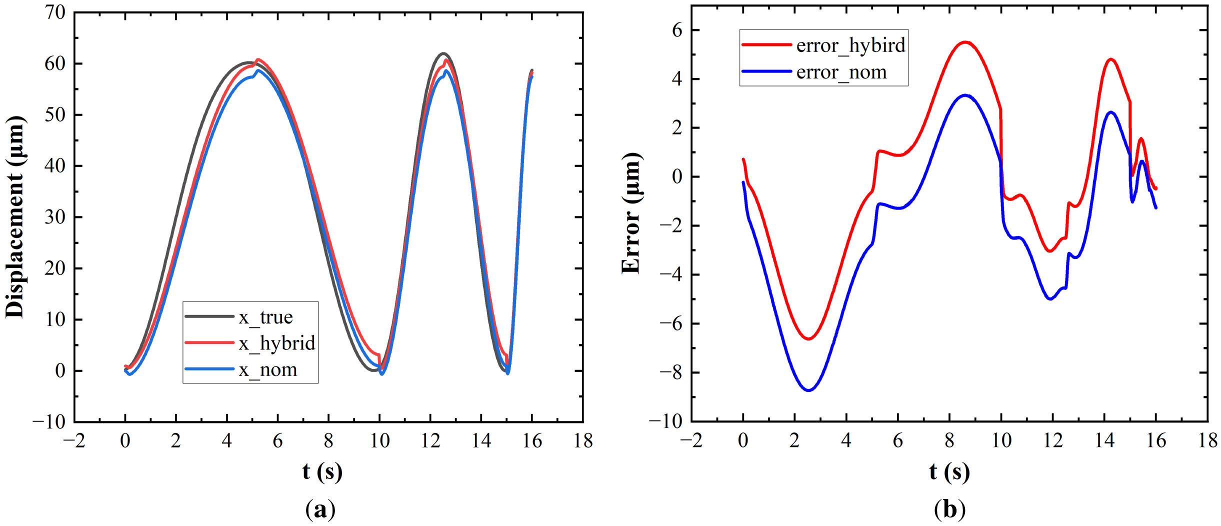

Figure 13: Time-domain tracking results evaluated on the test set. (**a**) Overview of the displacement tracking process; (**b**) Specific tracking error curves.

As can be seen, although the nominal physical model accurately reproduces the overall trend, slight deviations persist at the inflection points of the displacement curve. This phenomenon is primarily due to the inability of the physical model to fully describe high-order dynamic friction and other complex nonlinear effects. In contrast, the results predicted by the hybrid model correspond much better to the actual experimental data. This clearly indicates that the neural network correctly learned the residual dynamics, which were unfortunately ignored by the purely physical model, and that it ultimately made very precise corrections to the results of the nominal model.

To quantitatively assess the final accuracy of the proposed model, we carefully calculated the RMSE value. Experimental data clearly show that the RMSE of the purely physical nominal model is 2.39 μm. However, after the successful introduction of neural network compensation, the RMSE of the Hybrid-PINN model drops sharply to 1.861 μm. This represents a significant improvement in accuracy, exceeding 28.4%. Therefore, this substantial reduction in dynamic residuals indicates the high efficiency of the Hybrid-PINN model we propose in this study.

4.5 Comparative Experiments and Discussion

To highlight the considerable advantages of the Hybrid-PINN framework proposed in the article, we conducted several comparative experiments with three common reference methods:

- Standard PINN (Std-PINN). This method directly uses a neural network to approximate the actual displacement. It integrates the physical equations into the loss function as regularization terms.
- Pure Neural Network Model. This approach relies exclusively on the neural network to learn the input-output relationship, without any prior physical knowledge.
- LSTM Model. Based on the well-known LSTM networks, this model learns the dynamic relationship between inputs and outputs. Like the pure neural network, it does not incorporate any prior physical knowledge during the learning process.

4.5.1 Model Accuracy and Convergence

We first carefully evaluated the predictive capability of these models for piezoelectric hysteresis loops on the standard test dataset. Fig. 14 primarily illustrates the hysteresis loop fitting results obtained by the different methods under a sinusoidal excitation of 80 V and 0.1 Hz.

As can be clearly seen in Fig. 14a, the standard PINN model exhibits a significant overall error and local distortion. This phenomenon is mainly due to the fact that piezoelectric dynamic equations constitute a stiff system problem. In this case, without a high-quality initial estimation, the standard PINN model is very likely to become trapped in local minima. Consequently, it becomes very difficult for the network to adaptively search for the optimal solution if it relies solely on the physical loss function.

Furthermore, Fig. 14b shows that, although the LSTM model can approximate the hysteresis loop profile, it nevertheless exhibits distinct non-physical oscillations. This is, in fact, an inherent limitation of purely data-driven methods. This may be related to the limited physical constraints in purely data-driven models and their sensitivity to local fluctuations in the training data.

Moreover, Fig. 14c clearly shows that, while the MLP model correctly reproduces the overall slope of the hysteresis loop, it nevertheless makes significant errors in predicting its width. This is primarily due to the fact that MLP is essentially a static, memoryless model. Consequently, it is very difficult to reproduce the complex historical dependence of piezoelectric materials if the prediction is based solely on the input voltage.

In contrast, the proposed Hybrid-PINN model (Fig. 14d) offers better agreement with the measured loop in this case. With the aid of the nominal physical model with equivalent attenuation correction, the method better represents the main structure and saturation tendency of the hysteresis loop. Furthermore, the neural network module plays a crucial role as a residual compensator. It reduces part of the residual mismatch that is not captured by the nominal physical model.

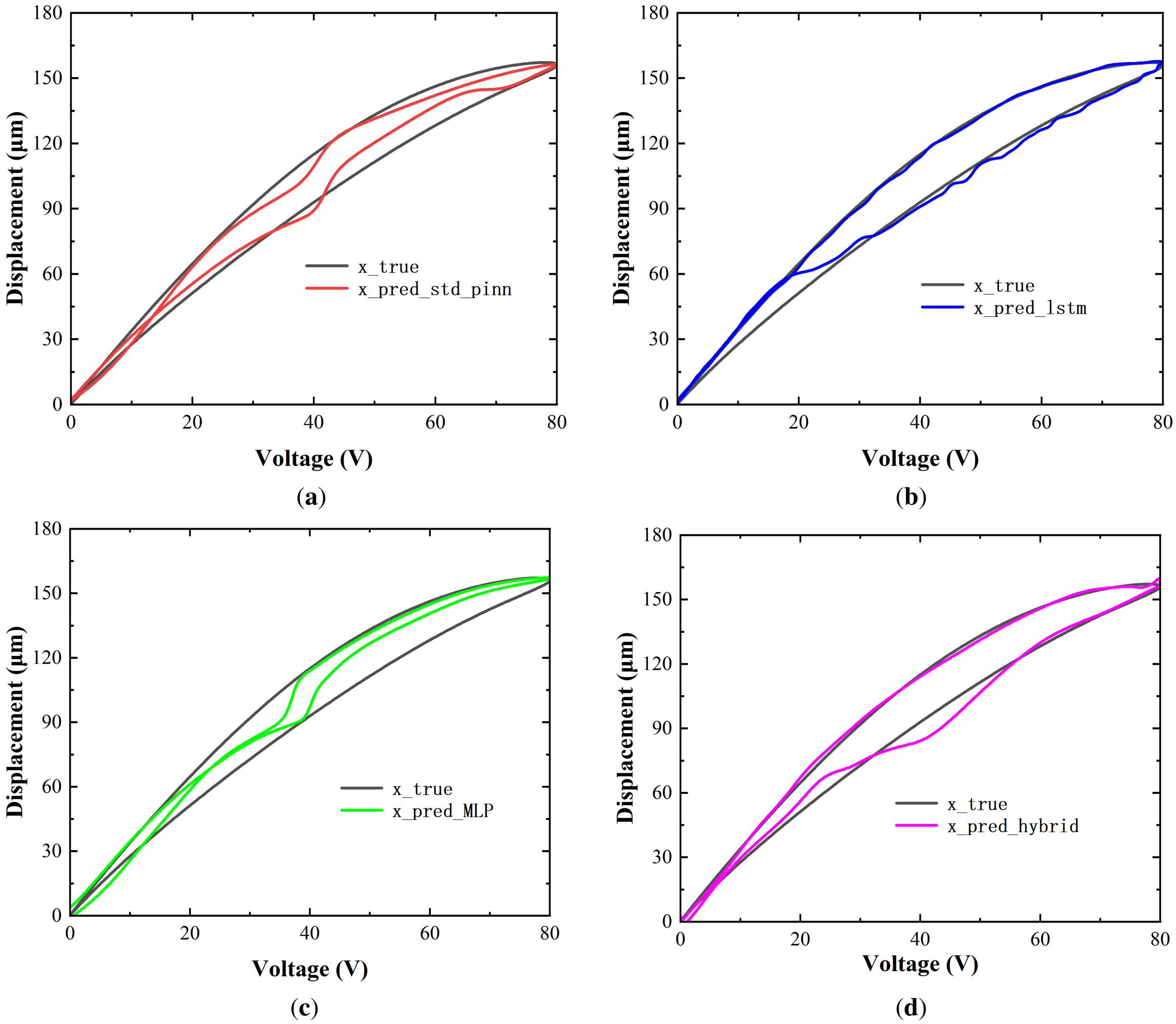

Figure 14: Comparison of hysteresis loop predictions between different models on the test set. (**a**) Std-PINN; (**b**) LSTM; (**c**) MLP; (**d**) Hybrid-PINN model.

Furthermore, Fig. 15 clearly compares the convergence rates of these different models throughout the training process.

Experimental results clearly indicate that the proposed Hybrid-PINN model achieves stable convergence in just 2000 epochs. In contrast, the loss values of the other reference models continue to oscillate at a relatively high level, even after 10,000 iterations. This significant disparity is primarily due to the high rigidity of the actuator, which reaches an order of magnitude of 10^7. Traditional reference models have enormous difficulty learning these rigid dynamics from scratch. The hybrid architecture uses the nominal physical model to represent the dominant dynamic trend, so the neural network mainly learns the remaining residual component.

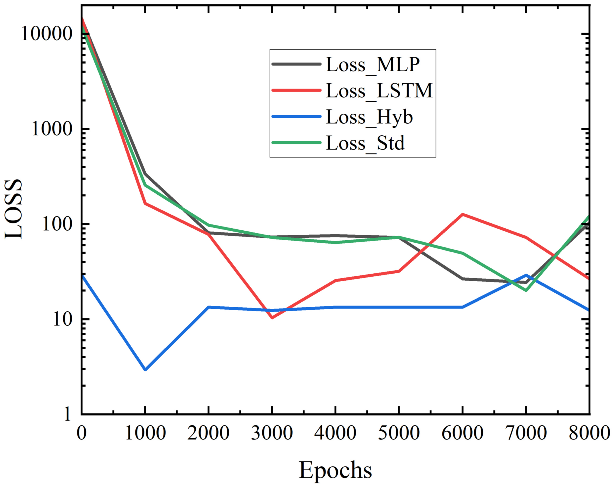

Figure 15: Comparative diagram of training residuals.

4.5.2 Data Efficiency

As is well known, acquiring long, high-precision datasets covering all operating conditions is often very complex during the practical deployment of precision positioning systems. The ability of a model to learn from small samples, therefore, becomes crucial. In this section, we use a random subsampling strategy to progressively reduce the size of the training set from 100% to 10%. This allows us to study in detail how the accuracy of the different models changes under these limited data scenarios.

Fig. 16 illustrates the evolution of the root mean square error (RMSE) for each model as a function of the training sample size. The MLP, standard PINN, and LSTM models all exhibit a strong data dependence. In other words, while their accuracy is acceptable with the full dataset, their prediction error increases exponentially when the sample size is drastically reduced to 10%. This phenomenon is primarily due to the lack of a priori physical constraints in these black-box models. Consequently, they are highly susceptible to overfitting due to high-frequency noise in the presence of sparse data. This results in a loss of their generalization capabilities.

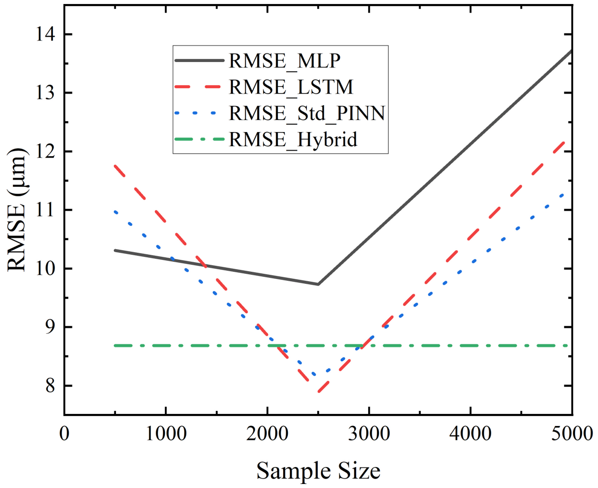

Figure 16: Impact of training data size on final prediction accuracy.

The Hybrid-PINN shows smaller variation in RMSE when the training sample size is reduced to 10%. This result suggests that the nominal physical model improves data efficiency within the measured operating range. However, this random subsampling test should not be interpreted as a complete validation under all sparse-data conditions.

4.5.3 Generalization Ability

To evaluate the condition-level prediction ability of the proposed model, several voltage–frequency cases were reserved as hold-out test conditions. These cases were not used during the training of the residual neural network. The resulting error distributions are shown in Figs. 17–20. More detailed error statistics for the hold-out operating conditions are provided in the Supplementary Materials.

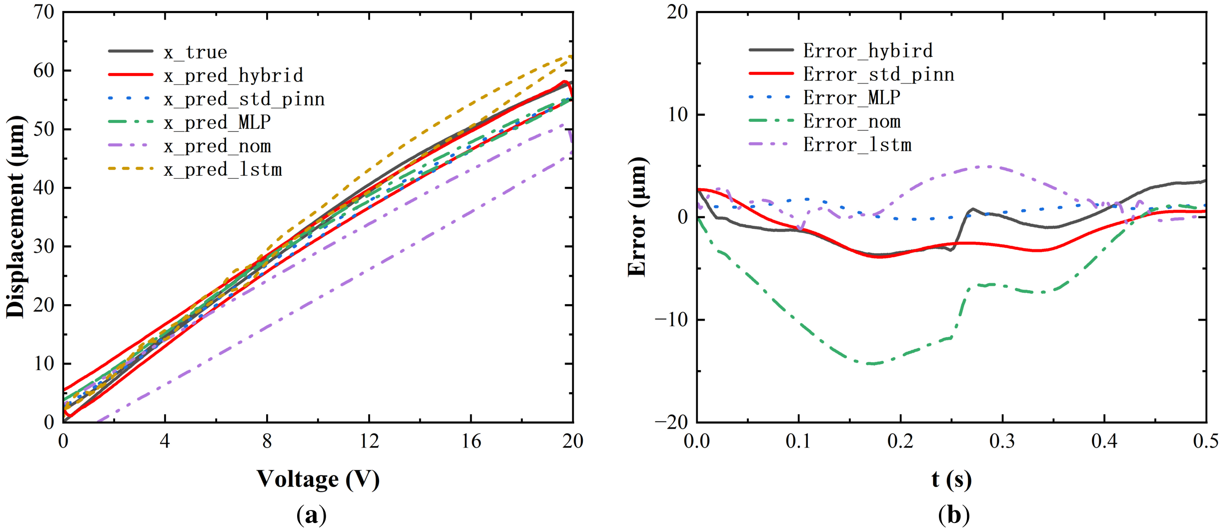

Figure 17: Comparison of hysteresis curves and tracking errors at 20 V/2 Hz. (**a**) Hysteresis loop; (**b**) Tracking error.

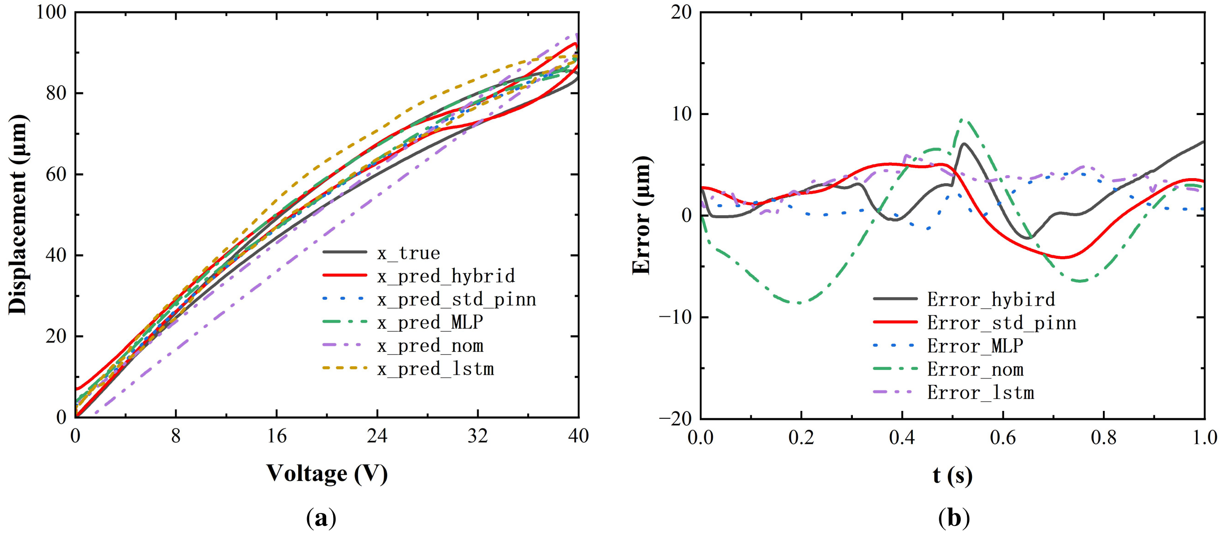

Figure 18: Comparison of hysteresis curves and tracking errors at 40 V/1 Hz. (**a**) Hysteresis loop; (**b**) Tracking error.

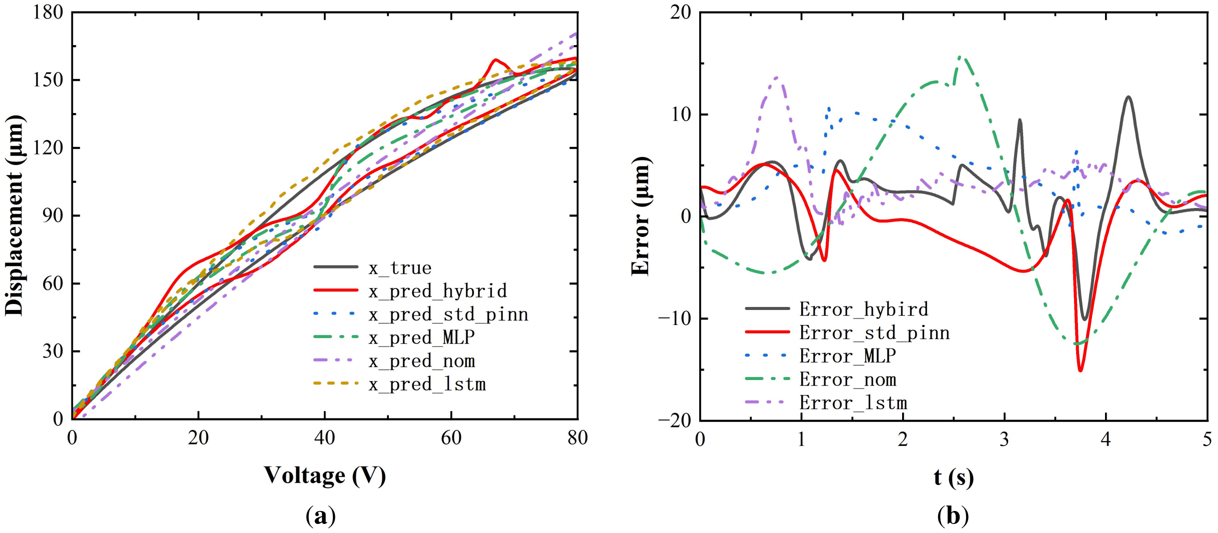

Figure 19: Comparison of hysteresis curves and tracking errors at 80 V/0.2 Hz. (**a**) Hysteresis loop; (**b**) Tracking error.

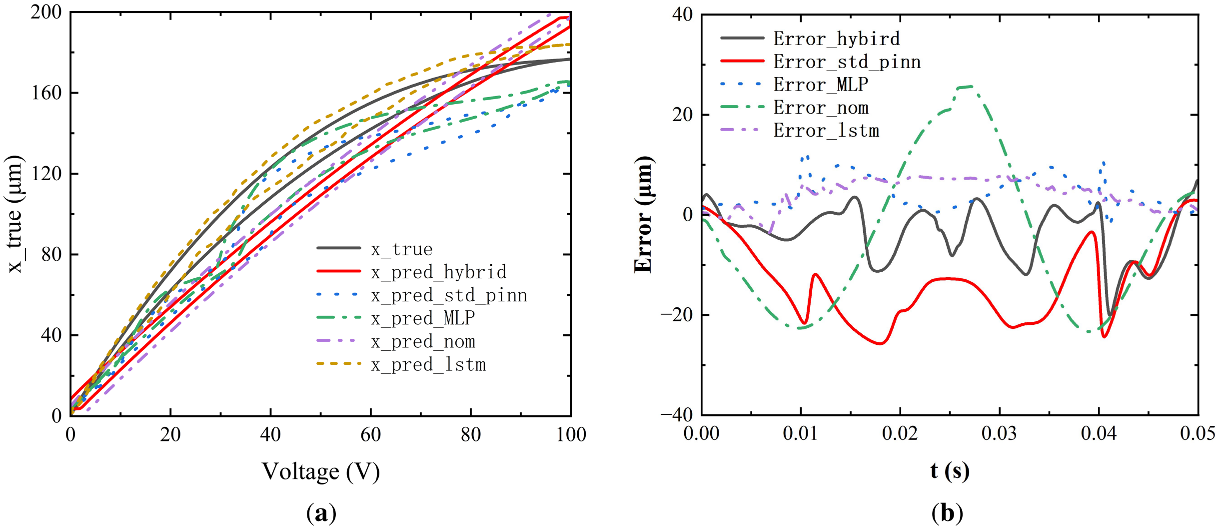

Figure 20: Comparison of hysteresis curves and tracking errors at 100 V/20 Hz. (**a**) Hysteresis loop; (**b**) Tracking error.

Table 4 presents the RMSE results for the five models under the aforementioned operating conditions.

Table 4: Results of the quantitative comparison of RMSE values.

	20 V, 2 Hz	**40 V, 1 Hz**	**80 V, 0.2 Hz**	**100 V, 20 Hz**
Physical Model	8.531	5.259	7.832	15.747
MLP	2.262	3.283	6.078	11.325
Std-PINN	2.317	3.187	4.063	15.645
LSTM	2.469	3.550	4.470	5.183
Hybrid-PINN	2.161	3.029	3.920	14.629

Experimental results show that the pure physical model and the MLP model exhibit the largest errors as a function of frequency. This is primarily due to their inability to model the influence of frequency on the width of the hysteresis loop. Meanwhile, while the LSTM model exhibits acceptable performance near the training frequencies, its prediction error increases significantly as the test frequency varies substantially. This is particularly true when extrapolated to unobserved high-frequency operating conditions.

As shown in Table 4, the Hybrid-PINN achieves the lowest RMSE in the 20 V/2 Hz, 40 V/1 Hz, and 80 V/0.2 Hz cases. However, in the 100 V/20 Hz case, the LSTM model obtains a lower RMSE than the Hybrid-PINN. This result indicates that the present nominal physical model and residual correction still have limitations in representing high-frequency rate-dependent dynamics. Therefore, the advantage of the proposed method should be interpreted mainly within the tested low- and medium-frequency cases, rather than as uniform superiority over all operating conditions.

The Hybrid-PINN model we proposed is not intended to replace those classical methods of nonlinear system identification under all circumstances. For those traditional methods, such as the nonlinear ARX, the Hammerstein-Wiener models, and the parametric models of Bouc-Wen type, they still remain highly useful when the structure of the model is clear enough. However, as for the actuator we tested in the experiment, the hysteresis, the saturation phenomenon of the output, the compliance of the lever, and those effects depending on the rate are coupled together. This kind of complex situation makes a purely parametric formulation less straightforward. Therefore, we can conclude that the main role of Hybrid-PINN is to make a combination between the low-order physical trend and the residual correction, which is driven by data.

The relatively lower accuracy of a purely physics-based model is partly because of its limited flexibility. As a low-order equivalent model, it is very hard for it to fully describe all those complex coupled effects of the actuator we tested. Besides, it cannot perfectly capture the saturation phenomenon. Therefore, the residual network in the framework provides a very necessary additional correction capability for these remaining model mismatches. Thus, this suggests that the improvement of the proposed Hybrid-PINN should be mainly attributed to the successful combination of the nominal physical trend and the residual correction, rather than simply relying on the expressiveness of the neural network alone.

The applicability of the proposed Hybrid-PINN is strictly limited to the configuration of the stacked actuator that we calibrated in the experiment. The nominal model is specially developed for an axial piezoelectric stack combined with a lever mechanism. Therefore, it cannot be directly transferred to those distributed piezoelectric patches or the bimorph structures. In those kinds of structures, the bending deformation, the strain depending on the curvature, and the modal coupling of the host-structure usually dominate the overall response [35]. For distributed piezoelectric patch systems used in active vibration control of flexible structures, the proposed residual-learning strategy could potentially be combined with modal reduced-order models or energy-density-based electromechanical formulations. In such cases, the neural residual branch may compensate for modal coupling, interface uncertainties, or frequency-dependent damping effects that are difficult to capture analytically. Related studies on distributed piezoelectric placement and modal decoupling in composite structures may provide a useful direction for extending the proposed framework.

The temperature drift phenomenon is not explicitly modeled in present study. Since the piezoelectric coefficients, the stiffness, the damping, and those hysteresis parameters may vary continuously along with the change of temperature, the residual network cannot be simply assumed to make a compensation for this kind of thermal drift, especially without the training data that is dependent on the temperature. However, the residual-learning branch could potentially compensate for moderate thermal variations if representative temperature-dependent training data are included. For larger environmental variations, additional physics terms or temperature-dependent parameters may be required in the nominal model.

Although the proposed attenuation term improves the representation of the measured saturation trend within the tested range, this does not mean that a universal physical mechanism has been established for untested high-voltage conditions. Therefore, if the model is to be applied beyond the calibrated voltage range in future work, additional experimental data at high voltage or a voltage-dependent attenuation formulation would be needed. The present work only validates the model within the calibrated operating range and does not claim reliable extrapolation capability beyond the training voltage.

5 Conclusions

This study presents a systematic modeling approach that combines mechanistic analysis and deep learning for piezoelectric actuators operating under large-stroke and dynamic conditions, with particular attention to output saturation and hysteresis nonlinearity. The proposed method integrates a low-order nominal physical model with a residual neural network, which aims to improve prediction accuracy while retaining a certain level of physical interpretability.

To address the output saturation observed in the displacement–voltage curve, an equivalent attenuation term is introduced into the nominal actuator-level model. This term is intended to describe the reduction of device-level actuation gain in the high-voltage and large-stroke region, rather than to propose a new material constitutive relation or redefine any universal piezoelectric constant. Experimental results show that the equivalent attenuation model provides a better representation of the measured saturation behavior within the calibrated operating range.

To further compensate for the residual mismatch that the nominal physical model cannot fully capture, a Hybrid-PINN architecture is proposed. This framework uses a parallel residual compensation strategy, where the physical model handles the main displacement trend and the neural network corrects the remaining unmodeled component. By embedding physical constraints into the loss function and applying a normalization procedure, the convergence difficulty caused by multi-physical quantity coupling is partly reduced.

Validation experiments were carried out on a precision micro-positioning platform. Results show that the Hybrid-PINN improves prediction accuracy over the nominal physical model by more than 20%. Compared with selected baseline models, the proposed method achieves lower prediction errors in most tested cases and shows better convergence behavior under the present experimental conditions. However, the proposed model does not outperform all baselines under every condition, which suggests that further improvement is still needed for high-frequency rate-dependent responses.

It should also be noted that this study is limited to the calibrated voltage–frequency range and tested environmental conditions. Temperature drift, operation beyond the calibrated voltage range, and end-to-end latency in real-time closed-loop implementation were not evaluated in the present work.

Acknowledgement: Not applicable.

Funding Statement: The authors received no specific funding for this study.

Author Contributions: The authors confirm contribution to the paper as follows: Conceptualization, Chenghao Kou and Shengjie Wang; methodology, Zunyi Duan and Chenghao Kou; software, Zhongwei Yang and Chenghao Kou; validation, Jun Ma and Xudong Tang; formal analysis, Rongchun Hu; investigation, Chenghao Kou; resources, Jun Ma; data curation, Zhongwei Yang; writing—original draft preparation, Chenghao Kou; writing—review and editing, Zunyi Duan; supervision, Shengjie Wang; project administration, Jun Ma. All authors reviewed and approved the final version of the manuscript.

Availability of Data and Materials: The original findings presented in this study are included in the current article. More detailed data can be obtained in the Supplementary Materials. Further inquiries can be directed to the corresponding author (Zunyi Duan).

Ethics Approval: Not applicable.

Conflicts of Interest: The authors declare no conflicts of interest.

Supplementary Materials: The supplementary material is available online at https://www.techscience.com/doi/10.32604/cmes.2026.083699/s1.

Abbreviations

The following abbreviations are used in this manuscript:

PEAs	Piezoelectric actuators
PINN	Physics-Informed Neural Network
Hybrid-PINN	Hybrid Physics-Informed Neural Network
RNNs	Recurrent neural networks
MLP	Multilayer perceptron
LSTM	Long Short-Term Memory
MAE	Mean absolute error
RMSE	Root mean square error
Std-PINN	Standard Physics-Informed Neural Network
NARX	Nonlinear autoregressive model with exogenous inputs

References

1. Wu T, Hu W, Zhang J, Zhang Z, Cheng C, Wu J, et al. Research on hysteresis modeling and nonlinear compensation of piezoelectric actuators. J Vibr Eng Technolog. 2025;13(1):52. doi:10.1007/s42417-024-01623-6.
2. Zhong E, Wang S, Zhai C, Li W. Improved non-singular fast terminal sliding mode control with hysteresis compensation for piezo-driven fast steering mirrors. Actuators. 2025;14(4):170. doi:10.3390/act14040170.
3. Zhang Y, Yan P. Disturbance observer-based robust optimal control of rate-dependent hysteretic systems: application to a piezoelectric nano-manipulator. Sens Actuators A Phys. 2024;366(5):114951. doi:10.1016/j.sna.2023.114951.
4. Masante A, Hecker R, Peña M. Sliding mode control with continuous switching function and adaptive compensation of hysteresis and disturbances for a piezoelectric flexure-stage. Int J Dyn Control. 2025;13(1):23. doi:10.1007/s40435-024-01537-x.
5. Jin J, Sun X, Chen Z. Comprehensive compensation of dynamic hysteresis and creep for piezoelectric actuator. Smart Mater Struct. 2024;33(6):065045. doi:10.1088/1361-665X/ad4e7d.
6. Yuan X, Wang B, Rong Y, Zou H, Wang W. Vibration suppression compound control of piezoelectric micro-displacement platform based on PI-BiRNN hysteresis model. J Vibr Eng Technolog. 2026;14(1):46. doi:10.1007/s42417-025-02260-3.
7. Sima J, Lai L, Fang Y, Zhu L. Coupled hysteresis and resonance control of three-degree-of-freedom tip-tilt-piston piezoelectric stage. Precis Eng. 2024;89(8):393–407. doi:10.1016/j.precisioneng.2024.07.001.
8. Dai Y, Li D, Wang D. Review on the nonlinear modeling of hysteresis in piezoelectric ceramic actuators. Actuators. 2023;12(12):442. doi:10.3390/act12120442.
9. Cai J, Dong W, Nagamune R. A survey of Bouc-Wen hysteretic models applied to piezo-actuated mechanical systems: modeling, identification, and control. J Intell Mater Syst Struct. 2023;34(16):1843–63. doi:10.1177/1045389x231157361.

10. Liu H, Zhang G. Establishment and evaluation of dynamic hysteresis models for piezo-positioning platform with high-frequency resonance characteristics. Measurement. 2026;258(1):119240. doi:10.1016/j.measurement.2025.119240.
11. Gu X, Yang W, Dong L, Zhou J. Investigation of hysteresis phenomena and compensation in piezoelectric stacks for active rotor. Actuators. 2025;14(7):327. doi:10.3390/act14070327.
12. Wang G, Zhou Y. A novel identification approach of Bouc–Wen model parameter for piezoelectric hysteresis characteristic based on a modified whale optimization algorithm. COMPEL. 2023;42(2):620–36. doi:10.1108/compel-05-2022-0173.
13. Li W, Liu K, Wang H, Deng Q, Yang Z. Study on dynamic hysteresis characteristic modeling and parameter identification methods for high-voltage piezoelectric actuators. JNWPU. 2025;43(3):610–9. doi:10.1051/jnwpu/20254330610.
14. Zhou M, Dai Z, Zhou Z, Liu X, Cao T, Li Z. Modeling, identification, and high-speed compensation study of dynamic hysteresis nonlinearity for piezoelectric actuator. J Intell Mater Syst Struct. 2024;35(9):822–44. doi:10.1177/1045389x231225492.
15. Zhu R, Liu L, Wu Y, Chen H, Lou W, Yang P, et al. Modeling and parameter identification of rate-dependent hysteresis behavior based on modified-generalized Prandtl–Ishlinskii model. Smart Mater Struct. 2024;33(7):075003. doi:10.1088/1361-665X/ad4d38.
16. Zhang Y, Ling J, Rakotondrabe M, Zhu Y, Wang D. Modeling and feedforward control of hysteresis in piezoelectric actuators considering its rotation and expansion. Mechatronics. 2025;110(9):103354. doi:10.1016/j.mechatronics.2025.103354.
17. Ling M, Wu S, Luo Z, Chen L, Huang T. An electromechanical dynamic stiffness matrix of piezoelectric stacks for systematic design of micro/nano motion actuators. Smart Mater Struct. 2023;32(11):115012. doi:10.1088/1361-665X/ace4aa.
18. Rosso M, Kohtanen E, Corigliano A, Ardito R, Erturk A. Dynamical behavior of frequency up-converted piezoelectric vibration energy harvesters at different velocities of magnetic interaction. In: Proceedings of the 2022 21st International Conference on Micro and Nanotechnology for Power Generation and Energy Conversion Applications (PowerMEMS); 2022 Dec 12–15; Salt Lake City, UT, USA. doi:10.1109/PowerMEMS56853.2022.10007622.
19. Rosso M, Kohtanen E, Corigliano A, Ardito R, Erturk A. Nonlinear phenomena in magnetic plucking of piezoelectric vibration energy harvesters. Sens Actuators A Phys. 2023;362:114667. doi:10.1016/j.sna.2023.114667.
20. Zhou C, Yuan M, Feng C, Ang WT. A modified Prandtl-ishlinskii hysteresis model for modeling and compensating asymmetric hysteresis of piezo-actuated flexure-based systems. Sensors. 2022;22(22):8763. doi:10.3390/s22228763.
21. Cheng Y, Liu J, Zhang X, Lu B. Gird-search-based neural network modeling of piezoelectric hysteresis for gravitational wave inertial sensor. Acta Astronaut. 2025;232(6):132–42. doi:10.1016/j.actaastro.2025.02.042.
22. Jin J, Sun X, Chen Z. Optimized neural network-based modeling of dynamic hysteresis in piezoelectric actuators. J Intell Mater Syst Struct. 2025;36(4):223–41. doi:10.1177/1045389x241300727.
23. Zhu B, Zhou M, Ren Y, Zhang X, Zhao Q, Wu W, et al. Hysteresis modeling of piezoelectric actuators based on neural network considering load and environmental stiffness. J Phys Conf Ser. 2024;2820(1):012095. doi:10.1088/1742-6596/2820/1/012095.
24. Lu J, Wang J, Bo Y, Liu Z. Hysteresis modeling and compensation of a piezoelectric fast steering platform using multiple NARMA-L2 models. Control Eng Pract. 2023;141(2):105695. doi:10.1016/j.conengprac.2023.105695.
25. Baziyad AG, Nouh AS, Ahmad I, Alkuhayli A. Application of least-squares support-vector machine based on hysteresis operators and particle swarm optimization for modeling and control of hysteresis in piezoelectric actuators. Actuators. 2022;11(8):217. doi:10.3390/act11080217.
26. Meng Y, Wang X, Li L, Huang W, Zhu L. Hysteresis modeling and compensation of piezoelectric actuators using Gaussian process with high-dimensional input. Actuators. 2022;11(5):115. doi:10.3390/act11050115.
27. Wang Y, Zhou M, Shen C, Cao W, Huang X. Time delay recursive neural network-based direct adaptive control for a piezo-actuated stage. Sci China Technol Sci. 2023;66(5):1397–407. doi:10.1007/s11431-022-2081-7.

28. Ahmed K, Yan P. Grey box inverse hysteresis modeling and control for piezo-actuated nano stages. J Mech Sci Technol. 2025;39(4):1711–8. doi:10.1007/s12206-025-0301-7.
29. Chen Y, Chen Y, Zheng L, Tong L, Chen W, Ji H. Nonlinear adaptive tracking control of piezoelectric bimorph actuator using hybrid modeling approach. Int J Appl Electromagn Mech. 2023;71(1_suppl):S403–12. doi:10.3233/jae-220187.
30. Ni L, Li Y, Yao N, Chen G, Zhang L, Wang G. A neuro-enhanced Duhem model and parameter identification using a modified *Gorilla* troops optimizer for generic piezoelectric hysteresis response. Sens Actuators A Phys. 2024;376(11):115651. doi:10.1016/j.sna.2024.115651.
31. Jin J, Sun X, Chen Z. Inverse feedforward control of piezoelectric actuators using optimized composite neural network-based Hammerstein model. J Intell Mater Syst Struct. 2024;35(20):1558–75. doi:10.1177/1045389x241286184.
32. Aggogeri F, Pellegrini N. Piezoelectric hysteresis modeling under a variable frequency based on a committee machine approach. Sensors. 2025;25(17):5371. doi:10.3390/s25175371.
33. Li H, van Duivenbode J, Ciuhu C, Lomonova EA. Understanding inertia and saturation in operational hysteresis through a physics-based piezo model. IET Sci Meas Technol. 2025;19(1):e70027. doi:10.1049/smt2.70027.
34. Leadenham S, Erturk A. Unified nonlinear electroelastic dynamics of a bimorph piezoelectric cantilever for energy harvesting, sensing, and actuation. Nonlinear Dyn. 2015;79(3):1727–43. doi:10.1007/s11071-014-1770-x.
35. Aksoy YT, Şahin M. Active vibration control of a smart sandwich plate via optimally located piezoelectric sensors and actuators. Results Eng. 2026;29(3):108513. doi:10.1016/j.rineng.2025.108513.